

Direct Demonstration of a Magnetic Dead Layer Resulting from A-Site Cation Inhomogeneity in a (La,Sr)MnO₃ Epitaxial Film System

Lei Jin,* Chun-Lin Jia, Ionela Lindfors-Vrejoiu, Xiaoyan Zhong, Hongchu Du, and Rafal E. Dunin-Borkowski

The degradation of the functional properties of epitaxial oxide films and the performance of related devices have often been attributed to the presence of so-called interfacial “dead layers”. Extensive efforts have been made to understand the origin of such dead layers and to avoid their formation. However, the results of these efforts have not been fully satisfactory, largely as a result of the complex origin of dead layers. Here, the dead layer is studied in a sample that contains hillocks of nominally La_{0.7}Sr_{0.3}MnO₃ (LSMO) sandwiched between a ferroelectric PbTiO₃ film and a Nb-doped SrTiO₃ substrate using aberration-corrected (scanning) transmission electron microscopy, nanobeam electron magnetic circular dichroism spectroscopy, and related techniques. The results here reveal the presence of a 5 nm thick layer in the LSMO hillocks, close to the LSMO/Nb-SrTiO₃ interface, which exhibits distinct structural and physical properties. The atomic, electronic, and magnetic structures and local chemistry of the interfacial layer are determined. It is found that octahedral rotations are suppressed in ultrathin regions at the edges of the hillocks, providing evidence for a strong effect of the adjacent Nb-SrTiO₃ and PbTiO₃. The formation of the dead layer is discussed in the light of lattice strain and valence changes of Mn ions.

1. Introduction

In epitaxial films of functional oxides, so-called “dead layers” often form near interfaces with other materials. The electrical and/or magnetic properties of such dead layers can deviate significantly from those of the corresponding bulk films, greatly

affecting the performance of devices.^[1–3] The formation of dead layers in colossal magnetoresistive manganite films appears to be independent of the choice of substrate, although their estimated thicknesses (which range from ≈1 to ≈10 nm) are found to depend on the substrate.^[4–10]

Re_{1-x}Ae_xMnO₃ manganites with perovskite structures (where Re is a trivalent rare-earth ion and Ae is a substituting divalent alkaline-earth ion) exhibit a variety of interesting properties, e.g., metal–insulator transitions, colossal magnetoresistance, and magnetocaloric behavior.^[11–13] LaMnO₃ ($x = 0$), one of the end compounds of the solid solutions, is an antiferromagnetic insulator ($T_N \approx 140$ K), with orbital order induced by the cooperative Jahn–Teller (JT) effect of Mn³⁺ ions below $T_{JT} \approx 750$ K.^[14] With increasing Sr substitution (resulting in hole doping), La_{1-x}Sr_xMnO₃ ($0 < x < 0.6$) gradually changes its room temperature behavior from that of a paramagnetic

insulator to a ferromagnetic metallic state, accompanied by a transition from an orthorhombic phase (O-phase) to a rhombohedral phase (R-phase) at $x \approx 0.2$.^[15–17]

Bulk La_{0.7}Sr_{0.3}MnO₃ (hereafter referred to as LSMO with $x \approx 0.3$) has a rhombohedral structure with space group $R\bar{3}c$.^[18] In the $R\bar{3}c$ structure, MnO₆ octahedra rotate in a way that can

Dr. L. Jin, Prof. C.-L. Jia, Prof. R. E. Dunin-Borkowski
Peter Grünberg Institute
Research Centre Jülich
D-52425 Jülich, Germany
E-mail: l.jin@fz-juelich.de

Dr. L. Jin, Prof. C.-L. Jia, Dr. H. C. Du,
Prof. R. E. Dunin-Borkowski
Ernst Ruska-Centre for Microscopy and Spectroscopy
with Electrons
Research Centre Jülich
D-52425 Jülich, Germany
Prof. C.-L. Jia
The School of Electronic and Information Engineering
Xi'an Jiaotong University
Xi'an 710049, China

Dr. I. Lindfors-Vrejoiu
II. Physics Institute
University of Cologne
D-50937 Cologne, Germany

Prof. X. Y. Zhong
Beijing National Center for Electron Microscopy
Laboratory of Advanced Materials and Department
of Materials Science and Engineering
Tsinghua University
Beijing 100084, China

Dr. H. C. Du
Central Facility for Electron Microscopy (GFE)
RWTH Aachen University
D-52074 Aachen, Germany



DOI: 10.1002/admi.201600414

be described by the Glazer notation aaa .^[19] Among the $\text{La}_{1-x}\text{Sr}_x\text{MnO}_3$ family (hereafter referred to as $(\text{La,Sr})\text{MnO}_3$), $x = 0.3$ corresponds to the highest Curie temperature T_C of about 370 K for the paramagnetic to ferromagnetic phase transition.^[15–17] Owing to its half-metallic nature^[20] and to the nearly full spin-polarized state^[21] of the charge carriers (holes), LSMO is often selected as the bottom electrode in thin film devices^[22–24] and as the active magnetic layer in magnetic tunnel junctions.^[25] LSMO films can be grown epitaxially on a wide range of commercially available substrates,^[4–10] including SrTiO_3 (STO), $(\text{LaAlO}_3)_{0.3}(\text{Sr}_2\text{AlTaO}_6)_{0.7}$, and NdGaO_3 .

The dead layer in LSMO thin films has been widely studied. Research efforts have been made to circumvent the formation of the dead layer, as well as to restore the functionalities of ultrathin LSMO films through interface engineering.^[26–29] One example is provided by superlattices of LSMO with layers as thin as 2 unit cells that are ferromagnetic.^[29] In this system, interfacing LSMO with ferromagnetic metallic layers of orthorhombic SrRuO_3 helps to preserve the tilts of LSMO oxygen octahedra and to maintain the ferromagnetic properties of LSMO layers that are as thin as 2 unit cells.

Nevertheless, in general the origin of the dead layer is still not clear. Deviation from chemical stoichiometry,^[30,31] lattice strain^[4] and interfacial structural coupling^[10] have all been suggested to play an important role in its formation, through electronic modification^[32] as well as field doping.^[33–37] The complex origin of the dead layer usually leads to difficulties in considering all possible contributing factors, rendering most existing studies incomplete.

Here, we present a detailed study of a dead layer in LSMO by means of transmission electron microscopy (TEM) and scanning TEM (STEM). We examine heterostructures consisting of hillock-like LSMO nanostructures sandwiched between a 50 nm thick ferroelectric PbTiO_3 (PTO) film and a semiconducting Nb-doped STO (Nb-STO) substrate. The thickness of the hillock-structured LSMO layer, which was deposited using a stencil technique,^[22,23] varies from the foot to the center of each hillock. This 3D hillock geometry (as shown in Figure 1 of ref. [23]) allows different thicknesses of the film to be investigated simultaneously. Our results reveal the presence of a distinct bottom layer, which differs from the bulk-like R-phase of LSMO present in the top parts of the hillocks in terms of its atomic structure, chemical composition, and electronic and magnetic properties and thus constitutes a dead layer. The formation of the dead layer and its influence on the formation of 180° ferroelectric domains in the adjacent PTO film are discussed.

2. Results

Figure 1a shows a representative STEM high-angle annular dark-field (HAADF) image of a cross-section of a LSMO hillock

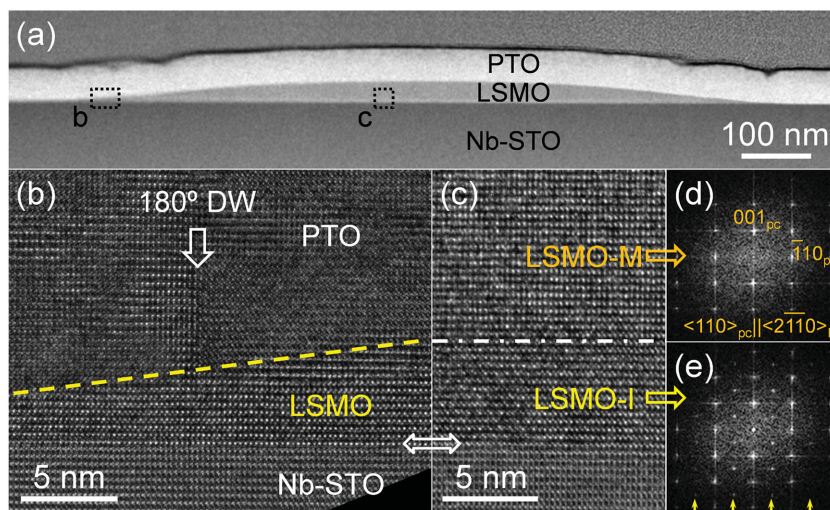


Figure 1. a) HAADF image showing the cross-sectional geometry of a LSMO hillock sandwiched between a continuous PTO thin film (about 50 nm thick with the brightest contrast) and a semiconducting Nb-STO substrate. b) HRTEM image showing the geometry at the foot (region “b” in (a)) of the LSMO hillock. An open arrow indicates a 180° domain wall in the PTO film. The dashed line and horizontal double-headed arrow mark the PTO/LSMO and LSMO/Nb-STO interfaces, respectively. c) HRTEM image showing an area of the interface between the LSMO film and the Nb-STO substrate at the central part of the hillock (region “c” in (a)). A 5 nm thick interfacial layer (LSMO-I) is visible below the dashed line. d) FFT of the LSMO film matrix (LSMO-M) above the dashed line in (c) viewed along the $\langle 110 \rangle_{pc}$ direction (pc: pseudocubic, $\parallel \langle 2\bar{1}\bar{1}0 \rangle_R$, see Figure S1a, Supporting Information). e) FFT of the LSMO-I layer, exhibiting additional reflection spots, as marked by the vertical arrows, which are not present in (d).

sandwiched between a PTO film and a Nb-STO substrate. The thickness of the hillock varies from 0 at its feet to ≈ 40 nm at its central part, forming a wedge-like shape at each side (see LSMO in Figure 1b). Domain walls (DWs) separating 180° ferroelectric domains are found to occur in the PTO film, depending on the thickness of the LSMO hillock layer.^[23]

Figure 1b,c shows high-resolution TEM (HRTEM) images recorded from regions of the sample denoted by frames “b” and “c” of Figure 1a, respectively, viewed along the $\langle 110 \rangle$ direction of Nb-STO. A 180° DW in the PTO film is marked by a vertical arrow in Figure 1b. The interface between PTO and LSMO is traced by a yellow dashed line, while that to the Nb-STO is denoted by a white double-headed arrow. In Figure 1b, the contrast of the LSMO layer looks essentially the same. The thickness of the LSMO layer in this area of the hillock foot is measured to be between 2.5 nm on the left and 5 nm on the right. In contrast, in Figure 1c, above the interface with the substrate a bottom layer of the LSMO hillock film (the area below the white dashed line, denoted LSMO-I), which has a uniform thickness of ≈ 5 nm, has slightly different contrast from that of the main part of the LSMO hillock (denoted LSMO-M, terminating at the PTO/LSMO interface). Figure 1d,e shows fast Fourier transform (FFT) images obtained from corresponding areas marked by open arrows in Figure 1c. The FFT patterns appear to be consistent with the $\langle 2\bar{1}\bar{1}0 \rangle_R$ and $\langle 10\bar{1}1 \rangle_R$ axes of LSMO, respectively (see Figure S1a, Supporting Information). In addition to the fundamental reflection spots shown in Figure 1d, extra spots (see arrows) are present at $(hkl)_{pc}$ ($h = k = n/2$, $n = \text{odd}$) positions in Figure 1e. An FFT of the LSMO layer shown in Figure 1b resulted in essentially the same

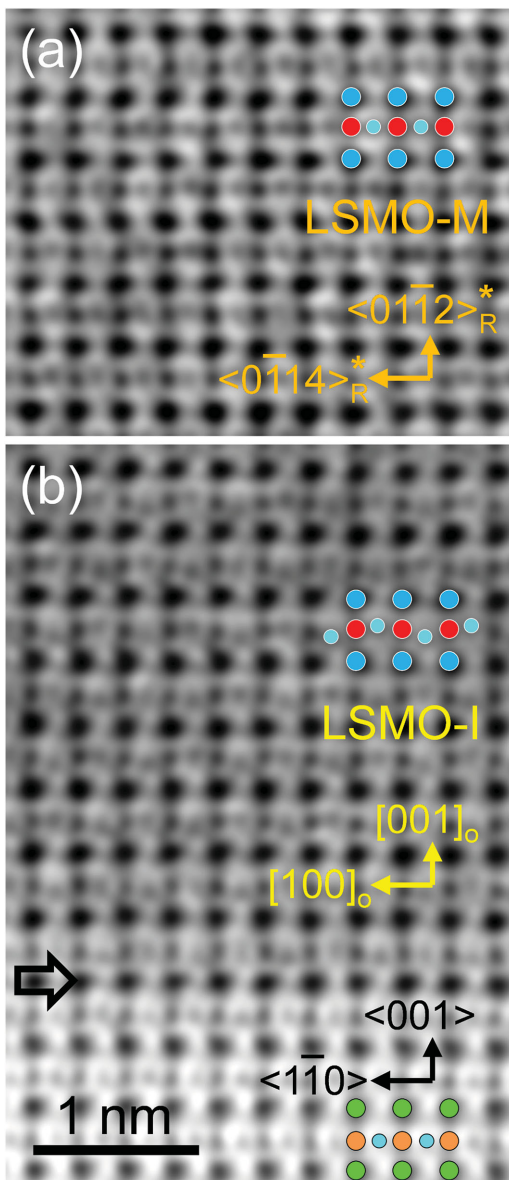


Figure 2. Atomic-resolution STEM ABF images acquired along the $\langle 110 \rangle$ direction of the Nb-STO substrate, showing the atomic structures of a) the LSMO-M film matrix and b) a region containing the LSMO-I layer and part of the Nb-STO substrate. The LSMO-I/Nb-STO interface is marked by a horizontal arrow. Atomic models are overlaid onto the two images, showing (La,Sr)O (light blue), SrO (green), Mn (red), Ti (orange), and O (small cyan dot). The semiconvergence angle of the electron beam is 21.4 mrad and the ABF collection angle is 12–24 mrad.

pattern as in Figure 1e, suggesting continuity of the bottom layer in the LSMO hillock. Indeed, this bottom layer is visible as a bright line at the LSMO/Nb-STO interface in the low magnification Z-contrast image shown in Figure 1a. It should be noted that the extra reflections become weak close to the end of the hillock feet.

Figure 2 shows atomic-resolution annular bright-field (ABF) images obtained from the central region of a LSMO hillock, including part of the LSMO-M region (Figure 2a) and part of the LSMO-I bottom layer and substrate (Figure 2b), recorded along

the $\langle 110 \rangle$ direction of Nb-STO. The images were denoised by using a nonlinear filtering algorithm.^[38] As indicated by the circles, all of the atomic columns, i.e., (La,Sr)O (light blue), SrO (green), Mn (red), Ti (orange), and O (small cyan dot) appear dark on a bright background. In the LSMO-I interfacial layer (Figure 2b) the oxygen positions are shifted alternately upward and downward parallel to $[001]_O$, as a result of rotations of the oxygen octahedra. In the Nb-STO substrate (Figure 2b) and the LSMO-M layer (Figure 2a), which extends to the LSMO/PTO interface, no rotation of oxygen octahedra is visible. The atomic-resolution details provide an interpretation of the appearance of noninteger reflection spots in the FFT image shown in Figure 1e. The octahedron rotation angles in the LSMO-I layer are measured to have an average value of $\approx 11.8^\circ \pm 1.4^\circ$ in the central part of the layer, which is $\approx 4^\circ$ larger than the rotation angle in the (La,Sr)MnO₃ R-phase (see the $\langle 10\bar{1}1 \rangle_R$ projection in Figure S1a, Supporting Information). This value is, however, comparable with the rotation angle of oxygen octahedra in the (La,Sr)MnO₃ O-phase (see the $[010]_O$ projection in Figure S1b, Supporting Information).

In order to verify the interpretation of the structures observed in the LSMO-I layer, details of the atomic structure were examined for the R- and O-phases. Following the symmetry breaking from the R- to the O-phase of (La,Sr)MnO₃ (Figure S1, Supporting Information), the threefold $\langle 02\bar{2}1 \rangle_R$ axes of the R-phase change correspondingly to the $[110]_O$, $[1\bar{1}0]_O$ and $[001]_O$ axes of the O-phase. In the latter case, the three axes are no more equivalent. The prominent difference in atomic structure is visible in both the $[110]_O$ and the $[1\bar{1}0]_O$ projections of the O-phase (Figure S1b, Supporting Information), in comparison with the projection of the R-phase structure along the equivalent $\langle 02\bar{2}1 \rangle_R$ direction (Figure S1a, Supporting Information): The A-site La/Sr cations are shifted upward and downward alternately, as denoted by the arrows in Figure S1b of Supporting Information. This feature leads to a periodicity of double perovskite units in real space and a double density of diffraction spots along $[001]_O$ in comparison with the R-phase (Figure S1a, Supporting Information). Furthermore, in the $[001]_O$ projection, adjacent oxygen octahedra rotate in an opposite sense, resulting in the presence of extra reflections in the center of the fundamental reciprocal lattice (see Figure S1b, Supporting Information). Experimentally, both features of the LSMO O-phase have been observed in the LSMO-I bottom layer (Figures S2–S4, Supporting Information).

Figure 3a shows a STEM ABF image of a LSMO hillock and part of the substrate viewed along the $\langle 010 \rangle$ direction of Nb-STO. Figure 3b displays an FFT generated from the entire image in Figure 3a. The FFT contains extra arrays of spots (marked by open arrows) that are a characteristic feature of the $[1\bar{1}0]_O$ diffraction pattern of the O-LSMO phase. An inverse FFT was performed by selecting the extra spots and used to generate a digital dark-field image (shown as an inset to Figure 3a), revealing the real space origin of the intensity in the extra spots, which matches the location of the LSMO-I bottom layer. The upward and downward shifts of the A-site cations are visible in the magnified image of the LSMO-I layer shown in Figure 3d, as denoted by the zigzag line, while such shifts do not occur in the LSMO-M layer (Figure 3c) or the Nb-STO substrate. All of these results provide evidence that a layer of the O-phase forms

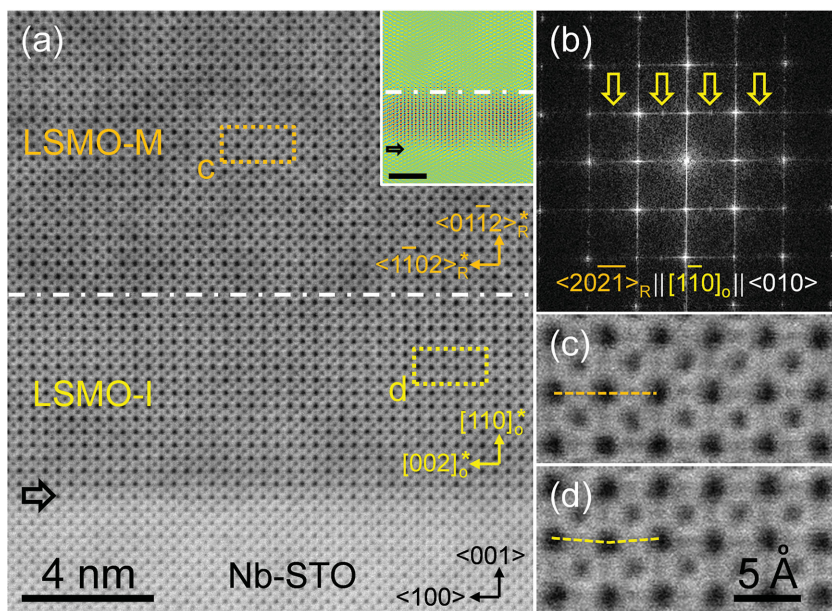


Figure 3. a) Low magnification STEM ABF image of the LSMO-I layer between the LSMO-M film matrix and the Nb-STO substrate. b) FFT of the three regions in (a), showing extra spots, as marked by open arrows. The inset to (a) shows an inverse FFT image formed by selecting the origin of only these reflections in real space. Scale bar: 4 nm. c,d) Magnified STEM ABF images obtained from the marked LSMO-M and LSMO-I regions, respectively. Zigzag features are seen in the A-site atom columns in (d), but not in (c) (see dashed lines).

in the LSMO hillock layer directly above the interface with the Nb-STO substrate.

The chemical composition of the O-phase bottom layer was investigated by using energy dispersive X-ray spectroscopy (EDXS) elemental mapping. **Figure 4a** shows net counts recorded from the La *L*, Sr *L*, Mn *K*, and Ti *K* peaks, averaged along the interface. A reduction in Sr *L* intensity occurs in the O-phase bottom layer, accompanied by an increase in La *L* and Mn *K* intensity (see distances ranging from -5 to 0 nm in **Figure 4a**). Cliff-Lorimer factors based on reference data from a 200 kV ChemiSTEM microscope were used to calculate atomic concentrations (at%). Since the difference in chemistry between the R- and O-phase is associated with the atomic ratio between La and Sr on the A-sites (**Figure S5**, Supporting Information), their relative ratio is given in **Figure 4b**. In the LSMO-M area (i.e., for distances from -8 to -5 nm), although the atomic concentration is not strictly homogeneous, the average La/Sr ratio from the profile is ≈ 2.53 (with a standard deviation $\sigma = 0.33$), which is consistent with the expected value for $\text{La}_{0.7}\text{Sr}_{0.3}\text{MnO}_3$ (La/Sr = 2.33). In the LSMO-I bottom layer, the La/Sr ratio increases to 3.84 ($\sigma = 0.43$) at the center of O-LSMO (i.e., for distances from -4.5 to -2.2 nm), corresponding to a stoichiometry close to $\text{La}_{0.8}\text{Sr}_{0.2}\text{MnO}_3$ ($x \approx 0.2$). We also measured the composition close to the tail of the foot of the LSMO hillock and found that the interfacial Sr-deficient bottom layer is always present.

Figure 5 shows an electron energy-loss spectroscopy (EELS) dataset acquired using the StripeSTEM technique^[39] from a similar area to that used for EDXS mapping. **Figure 5a** shows a STEM HAADF image of the sample area, from which the EELS spectra were acquired. **Figure 5b** shows the fine structure of the

O *K* edge, as extracted from the StripeSTEM dataset. Three prominent peaks, labeled “A”, “B”, and “C”, are present. In order to improve the signal-to-noise ratio, the spectra were integrated from EELS signals recorded from 5 perovskite unit cells, as indicated by the color braces in **Figure 5a**. The position of peak “A” recorded from the LSMO hillock shifts toward the low energy-loss direction with values of ≈ 0.4 eV (red) and 0.8 eV (magenta) in the LSMO-I layer and 1.0 eV (blue, olive, cyan) in the LSMO-M region. These peak shifts have been reported to be highly related to an increased Mn valence state.^[40] Meanwhile, peak “B” in the LSMO-I layer shifts by 0.4 eV to lower energy-loss, in comparison with those recorded from the LSMO-M area, manifesting a distinct change in Sr (or La) concentration from the O-phase to the R-phase of $(\text{La,Sr})\text{MnO}_3$.^[41] Since the Mn valency changes concomitantly with the local Sr (or La) concentration,^[41] it can be determined approximately from the energy difference ΔE between peaks “A” and “B” in **Figure 5b**, as reported by Riedl et al.^[42] In the R-phase matrix layer, the energy difference is 5.6 eV, corresponding to a mixed Mn valency of 3.3+ (according to Riedl et al.^[42])

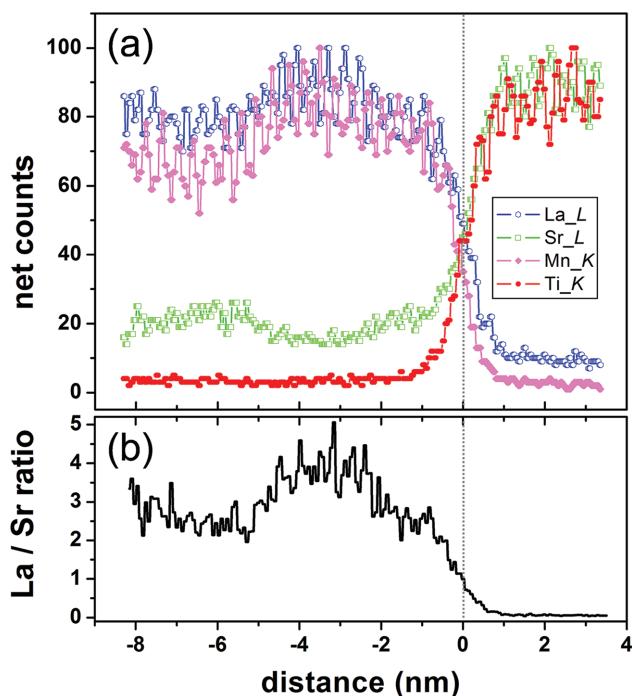


Figure 4. EDXS results for La *L*, Sr *L*, Mn *K*, and Ti *K* shells taken from the area shown in **Figure 2a**. a,b) The net counts and atomic concentration, respectively, plotted as a function of distance, obtained by averaging the EDXS results along the interface. The interface is marked by a vertical line. A Sr-deficient region, corresponding to the interfacial LSMO-I layer in **Figure 2a**, is seen to the left of the interface.

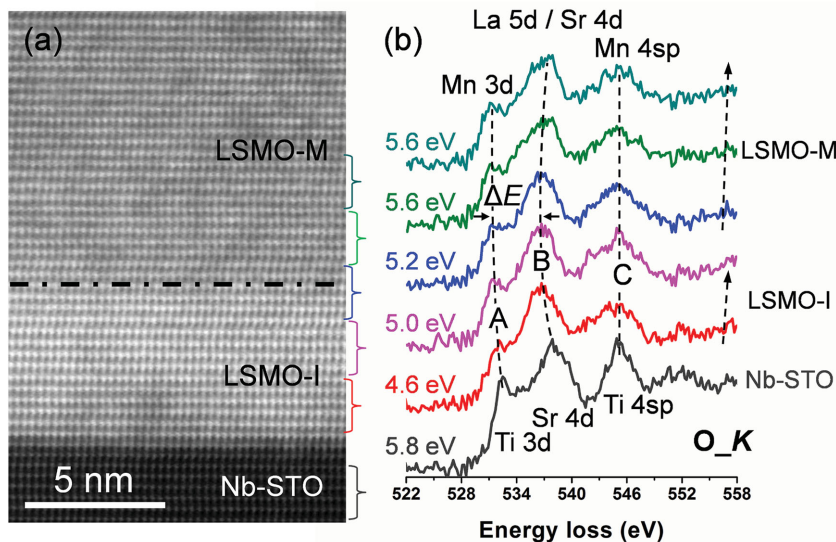


Figure 5. StripeSTEM dataset, comprising a) a STEM HAADF image and b) corresponding fine structures of O *K* edges. Three prominent peaks, labeled “A”, “B”, and “C”, are visible in (b). Peaks “A” and “C” are hybridizations of the O *2p* states with the transition metal (i.e., Ti and Mn) *3d* and *4sp* states, respectively, while peak “B” is characteristic of O *2p* states hybridized with Sr *4d* or La *5d* states. The energy difference ΔE between peaks “A” and “B” were measured to determine the Mn valency. The probe semiconvergence angle, inner HAADF detector angle, and spectrometer collection angle were 25, 70, and 21 mrad, respectively.

This value is consistent with nominal LSMO with $x = 0.3$ (Mn valency 3.3+). In the interfacial O-phase LSMO, ΔE ranges between 4.6 and 5.2 eV, which are comparable to the value of 4.8 eV as reported by Riedl et al.^[42] for an average Mn valence state of 3.175+ ($x = 0.175$). The EELS results therefore corroborate the conclusion of the formation of the LSMO O-phase.

The local magnetic properties of the LSMO-M and LSMO-I layers were tested by means of electron magnetic circular dichroism (EMCD),^[43,44] which was implemented using a nanobeam setting in STEM mode.^[45] The beam size used was ≈ 2.5 nm and the semiconvergence angle was ≈ 0.5 mrad. **Figure 6** displays background-subtracted EELS results from the Mn *L*_{2,3} and La *M*_{4,5} edges obtained for two chiral positions “+” and “−” (as shown in red and black, respectively) and corresponding EMCD spectra (i.e., intensity differences between the “−” and “+” spectra, shown in cyan) from the LSMO-M (Figure 6a) and interfacial LSMO-I (Figure 6b) regions, respectively. As expected, there is no EMCD signal present from the *M*_{4,5} edges of nonmagnetic La atoms in either the LSMO-M or the LSMO-I area. Experimental EMCD spectra contain contributions from both the intrinsic magnetic circular dichroism of magnetic materials and the dynamical diffraction conditions used.^[44] In order to compare the intrinsic magnetic circular dichroism of Mn atoms in the LSMO-M and LSMO-I areas, the differences between their dynamical diffraction coefficients were minimized by selecting the same diffraction conditions (see Figure 6b) and similar sample thicknesses. Significant EMCD signals are present at the Mn *L*_{2,3} edges in the LSMO-M area, while they are hardly detectable at the Mn *L*_{2,3} edges in the LSMO-I area. It is therefore experimentally demonstrated that the saturation magnetization is mostly suppressed in the interfacial bottom layer, since LSMO is saturated in the ≈ 2 T

magnetic field of the objective lens. When correlated with the EDXS and energy-loss near-edge structure (ELNES) data, our results show a concomitant decrease in saturation magnetization and Mn valency with the diminution of the Sr concentration in the LSMO-I interfacial layer. Therefore, the LSMO-I bottom layer can be regarded, in a real sense, as an electrically and magnetically dead layer at room temperature.

3. Discussion

Our results provide evidence for a structural R- to O-phase separation/transition at the LSMO/Nb-STO interface. The formation of the O-phase (i.e., LSMO-I) is associated with a deviation in local chemistry from the stoichiometric value of $x = 0.3$ for the A-site cations (i.e., between La and Sr). Similar cationic segregation was also reported in a Ca-doped manganite thin film grown on a STO (001) substrate.^[46] The structural change results in a distinct deterioration of the electronic and magnetic properties of the interfacial bottom layer.

The interfacial LSMO-I bottom layer, which has an increase in Mn³⁺ and a decrease in magnetization, is consistent with the definition of a “dead layer” (or critical thickness) in manganite thin films.^[7–9] For instance, Huijben et al.^[7] reported a critical thickness of ≈ 8 unit cells for metallic conductivity and 3 unit cells for ferromagnetism in La_{0.7}Sr_{0.3}MnO₃ thin films grown on an STO (001) substrate. By using X-ray magnetic circular dichroism and spectroscopic and scattering techniques, Lee et al. observed an intermediate layer with a thickness of ≈ 8 unit cells at a natural La_{0.7}Sr_{0.3}MnO₃/STO interface (i.e., an interface at which a different La/Sr ratio had not been introduced deliberately) and revealed that this layer has an increase in Mn³⁺, probably due to charge transfer and/or a doping instability.^[8]

It has been proposed that Mn ions play an important role in determining the unit cell volume of manganite perovskites,^[47] given the fact that the ionic radius of Mn³⁺ (65 pm) > Mn⁴⁺ (53 pm) and La³⁺ (136 pm) < Sr²⁺ (144 pm).^[48] With decreasing Sr concentration, more A-sites are occupied by La³⁺ ions. In order to maintain electric neutrality, some Mn⁴⁺ will change to Mn³⁺.^[47] The pseudo-cubic lattice parameter a_{pc} for La_{0.7}Sr_{0.3}Mn³⁺_{0.7}Mn⁴⁺_{0.3}O₃ (e.g., La_{0.8}Sr_{0.2}MnO₃, $a_{pc} \approx 3.89$ Å^[15]) is larger than that of La_{0.7}Sr_{0.3}Mn³⁺_{0.7}Mn⁴⁺_{0.3}O₃ ($a_{pc} \approx 3.88$ Å.^[15]) Therefore, an increase in lattice parameter associated with an increase in Mn³⁺ concentration (i.e., with the formation of a local O-phase) can reduce mismatch strain in the R-phase LSMO/Nb-STO system.

We note that the strong extra reflections corresponding to the O-phase become weak in areas close to the ends of the hillock feet, implying that octahedral rotations in such areas are strongly suppressed. The suppression of octahedral tilt was seen directly using STEM ABF imaging (Figure S6, Supporting Information). The suppression of octahedral rotations can be

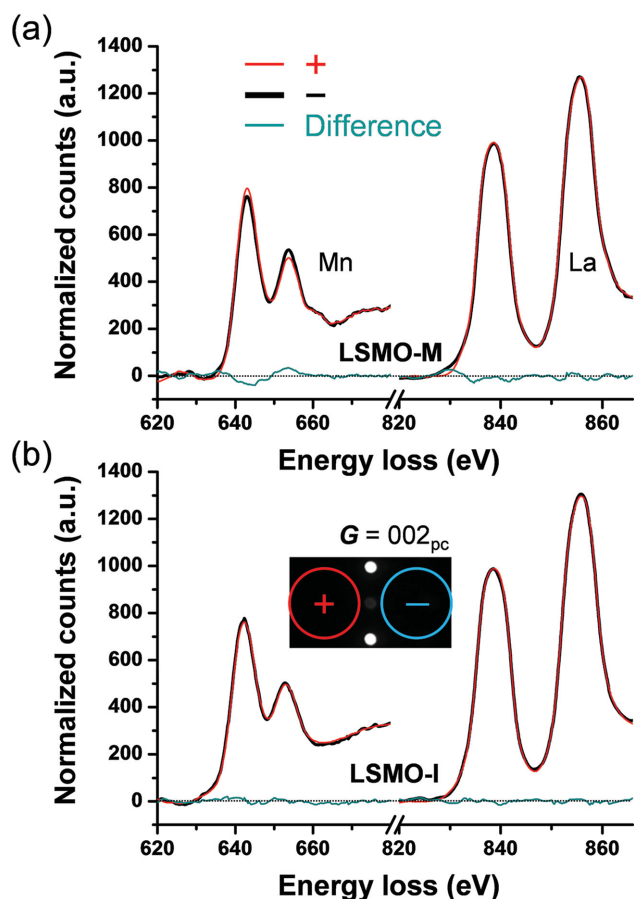


Figure 6. Smoothed nanobeam EMCD spectra recorded in a two-beam condition with pseudo-cubic $G = \{002\}_{pc}$ reflection exited from a) the LSMO-M film matrix and b) the interfacial LSMO-I layer. The diffraction pattern in (b) shows a typical two-beam condition, which was realized by tilting the sample $\approx 8^\circ$ away from the $\langle 110 \rangle_{pc}$ Laue zone axis. The positions of the EELS entrance aperture are shown schematically.

attributed to oxygen octahedral coupling of ultrathin LSMO with the non-tilted Nb-STO substrate and PTO film ($a^0a^0a^0$ in Glazer notation.^[19]) In particular, it was demonstrated by Moon et al.^[10] that functionalities such as electrical resistivity and magnetoresistance in ultrathin manganite films are affected significantly by interfacial structural coupling of oxygen octahedra (although local chemical information in individual samples was not provided). These findings were supported by density functional theory calculations.^[10] Our present atomic-resolution results, thereby, provide direct experimental evidence for such coupling in ultrathin manganite films.

In our previous work,^[23] we demonstrated a direct relationship between the formation of 180° ferroelectric domains and LSMO hillocks. This relation can now be understood in terms of the formation of the O-phase. Across the LSMO hillocks, the PTO thin film contacts three parts of the “substrate”: (1) the Nb-STO semiconducting substrate; (2) the Sr-deficient insulating LSMO interface layer (i.e., the O-phase layer with a thickness of ≈ 5 nm); (3) the main part of the LSMO hillock (i.e., the conducting LSMO R-phase matrix). The formation of 180° ferroelectric domains above the insulating O-phase can

reduce the system energy induced by the depolarization field at the interfaces.

4. Conclusion

By using several (scanning) transmission electron microscopy techniques, we have revealed the presence of an interfacial layer in $\text{La}_{0.7}\text{Sr}_{0.3}\text{MnO}_3$ hillocks. The interfacial layer shows structural features similar to those of the $\text{La}_{0.8}\text{Sr}_{0.2}\text{MnO}_3$ O-phase. The associated phase separation correlates with the formation of 180° ferroelectric domains in the adjacent PTO film. Our results demonstrate that such a novel hillock geometry can provide a useful platform for further studies of the thickness-dependent interfacial phenomena in epitaxial oxide heterostructures, which are also important in other ferroelectric and magnetic systems. They also show that aberration-corrected (scanning) transmission electron microscopy and spectroscopy are very powerful tools for detecting local variations in structural, compositional, electronic, and magnetic properties.

5. Experimental Section

Nb-STO/LSMO/PTO heterostructures were grown via a two-step procedure by pulse laser deposition (PLD), as reported by Vrejoiu et al.^[22] Briefly, nominally $\text{La}_{0.7}\text{Sr}_{0.3}\text{MnO}_3$ hillocks were grown by PLD at 600°C in an oxygen pressure of 2.7×10^{-2} mbar through a stencil mask that was mechanically attached to the surface of the Nb-STO substrate. After removing the stencil, the LSMO/Nb-STO structure was reheated to 585°C and a 50 nm thick PTO film was then deposited onto the same area in 0.25 mbar O_2 .

Cross-sectional specimens across areas that included the hillocks were prepared for TEM and STEM examination using focused ion beam (FIB) milling in an FEI Helios Nanolab 400s dual-beam system.^[49] More than 15 FIB lamellae were cut in Nb-STO $\langle 100 \rangle$ and $\langle 110 \rangle$ orientations (see ref. [23] for detailed information) for statistic evaluation and further polished using a 500 eV Ar ion-beam (Fischione Nanomill, Model 1040), in order to remove the damaged layers introduced by FIB milling.

HRTEM investigations were performed on an FEI Titan-T 80–300 transmission electron microscope with a spherical aberration (C_s) correction system for the objective lens, operated at an acceleration voltage of 300 kV.^[50] Investigations based on STEM techniques, including nanobeam electron diffraction,^[45] EMCD,^[43,44] ABF^[51] and HAADF imaging,^[52] and StripeSTEM,^[39] were carried out at 200 kV on an FEI Titan G3 60–300 “PICO” microscope equipped with a high-brightness field emission gun (XFEG), a monochromator unit, a probe C_s corrector and a combined image C_s-C_c (chromatic aberration) corrector,^[53] as well as at 300 kV on an FEI Titan 80–300 scanning transmission electron microscope equipped with a probe C_s correction system.^[54] EDXS mapping was performed on an FEI Titan G2 80–200 ChemiSTEM microscope equipped with an XFEG, a probe C_s corrector, and a super-X EDXS system.^[55]

Supporting Information

Supporting Information is available from the Wiley Online Library or from the author.

Acknowledgements

The authors thank Doris Meertens for specimen preparation by focused ion beam milling, Manuel Bornhöft for the nanobeam settings,

Zechao Wang for processing the EMCD spectra and performing the EMCD dynamical diffraction calculations, and Lothar Houben, Zi-An Li, and Dongsheng Song for helpful discussions. C.L.J. acknowledges support from the National Natural Science Foundation of China under Grant No. 51390472 and the National 973 Project of China (2015CB654903). X.Y.Z. acknowledges support from the National 973 Project of China (2015CB921700) and National Natural Science Foundation of China (51471096 and 51390471). H.C.D. acknowledges support from the Deutsche Forschungsgemeinschaft (SFB 917). The research leading to these results had received funding from the European Research Council under the European Union's Seventh Framework Programme (FP7/2007-2013)/ERC Grant Agreement No. 320832.

Received: May 11, 2016

Revised: June 27, 2016

Published online: July 20, 2016

- [1] M. Stengel, N. A. Spaldin, *Nature* **2006**, *443*, 679.
- [2] M. Stengel, D. Vanderbilt, N. A. Spaldin, *Nat. Mater.* **2009**, *8*, 392.
- [3] Y. Wang, M. K. Niranjan, K. Janicka, J. P. Velev, M. Ye. Zhuravlev, S. S. Jaswal, E. Y. Tsybal, *Phys. Rev. B* **2010**, *82*, 094114.
- [4] J. Z. Sun, D. W. Abraham, R. A. Rao, C. B. Eom, *Appl. Phys. Lett.* **1999**, *74*, 3017.
- [5] R. P. Borges, W. Guichard, J. G. Lunney, J. M. D. Coey, F. Ott, *J. Appl. Phys.* **2001**, *89*, 3868.
- [6] B. Kim, D. Kwon, T. Yajima, C. Bell, Y. Hikita, B. G. Kim, H. Y. Hwang, *Appl. Phys. Lett.* **2011**, *99*, 092513.
- [7] M. Huijben, L. W. Martin, Y. H. Chu, M. B. Holcomb, P. Yu, G. Rijnders, D. H. A. Blank, R. Ramesh, *Phys. Rev. B* **2008**, *78*, 094413.
- [8] J. S. Lee, D. A. Arena, P. Yu, C. S. Nelson, R. Fan, C. J. Kinane, S. Langridge, M. D. Rossell, R. Ramesh, C. C. Kao, *Phys. Rev. Lett.* **2010**, *105*, 257204.
- [9] H. Boschker, J. Kautz, E. P. Houwman, W. Siemons, D. H. A. Blank, M. Huijben, G. Koster, A. Vailionis, G. Rijnders, *Phys. Rev. Lett.* **2012**, *109*, 157207.
- [10] E. J. Moon, P. V. Balachandran, B. J. Kirby, D. J. Keavney, R. J. Sichel-Tissot, C. M. Schlepütz, E. Karapetrova, X. M. Cheng, J. M. Rondinelli, S. J. May, *Nano Lett.* **2014**, *14*, 2509.
- [11] M. B. Salamon, M. Jaime, *Rev. Mod. Phys.* **2001**, *73*, 583.
- [12] M. H. Phan, S. C. Yu, *J. Mag. Mag. Mater.* **2007**, *308*, 325.
- [13] L. P. Gor'kov, V. Z. Kresin, *Phys. Rep.* **2004**, *400*, 149.
- [14] J. B. Goodenough, A. Wold, R. J. Arrott, N. Menyuk, *Phys. Rev.* **1961**, *124*, 373.
- [15] A. Urushibara, Y. Moritomo, T. Arima, A. Asamitsu, G. Kido, Y. Tokura, *Phys. Rev. B* **1995**, *51*, 14103.
- [16] J. Hemberger, A. Krimmel, T. Kurz, H. A. Krug von Nidda, V. Yu. Ivanov, A. A. Mukhin, A. M. Balbashov, A. Loidl, *Phys. Rev. B* **2002**, *66*, 094410.
- [17] A. Szewczyk, M. Gutowska, B. Dabrowski, *Phys. Rev. B* **2005**, *72*, 224429.
- [18] S. J. Hibble, S. P. Cooper, A. C. Hannon, I. D. Fawcett, M. Greenblatt, *J. Phys. Condens. Matter* **1999**, *11*, 9221.
- [19] A. M. Glazer, *Acta Cryst. B* **1972**, *28*, 3384.
- [20] J. H. Park, E. Vescovo, H. J. Kim, C. Kwon, R. Ramesh, T. Venkatesan, *Nature* **1998**, *392*, 794.
- [21] M. Bowen, M. Bibes, A. Barthélémy, J. P. Contour, A. Anane, Y. Lemaître, A. Fert, *Appl. Phys. Lett.* **2003**, *82*, 233.
- [22] I. Vrejoiu, A. Morelli, F. Johann, D. Biggemann, *Appl. Phys. Lett.* **2011**, *99*, 082906.
- [23] L. Jin, C. L. Jia, I. Vrejoiu, *Appl. Phys. Lett.* **2014**, *105*, 132903.
- [24] Y. M. Kim, A. Kumar, A. Hatt, A. N. Morozovska, A. Tselev, M. D. Biegalski, I. Ivanov, E. A. Eliseev, S. J. Pennycook, J. M. Rondinelli, S. V. Kalinin, A. Y. Borisevich, *Adv. Mater.* **2013**, *25*, 2497.
- [25] L. Samet, D. Imhoff, J. L. Maurice, J. P. Contour, A. Gloter, T. Manoubi, A. Fert, C. Colliex, *Eur. Phys. J. B* **2003**, *34*, 179.
- [26] H. Yamada, Y. Ogawa, Y. Ishii, H. Sato, M. Kawasaki, H. Akoh, Y. Tokura, *Science* **2004**, *305*, 646.
- [27] Y. H. Liu, J. Xiong, J. T. Haraldsen, L. Yan, A. V. Balatsky, Q. X. Jia, A. J. Taylor, D. Yarotski, *Phys. Rev. B* **2013**, *87*, 165140.
- [28] O. Shapoval, S. Hühn, J. Verbeeck, M. Jungbauer, A. Belenchuk, V. Moshnyaga, *J. Appl. Phys.* **2013**, *113*, 17C711.
- [29] M. Ziese, F. Bern, E. Pippel, D. Hesse, I. Vrejoiu, *Nano Lett.* **2012**, *12*, 4276.
- [30] F. Song, Å. F. Monsen, Z. S. Li, J. W. Wells, E. Wahlström, *Surf. Interface Anal.* **2013**, *45*, 1144.
- [31] L. F. Kourkoutis, J. H. Song, H. Y. Hwang, D. A. Muller, *Proc. Natl. Acad. Sci. USA* **2010**, *107*, 11682.
- [32] J. A. Mundy, Y. Hikita, T. Hidaka, T. Yajima, T. Higuchi, H. Y. Hwang, D. A. Muller, L. F. Kourkoutis, *Nat. Commun.* **2014**, *5*, 3464.
- [33] X. Hong, A. Posadas, A. Lin, C. H. Ahn, *Phys. Rev. B* **2003**, *68*, 134415.
- [34] X. Hong, A. Posadas, C. H. Ahn, *Appl. Phys. Lett.* **2005**, *86*, 142501.
- [35] X. Hong, J. B. Yau, J. D. Hoffman, C. H. Ahn, *Phys. Rev. B* **2006**, *74*, 174406.
- [36] L. Jiang, W. S. Choi, H. Jeon, T. Egami, H. N. Lee, *Appl. Phys. Lett.* **2012**, *101*, 042902.
- [37] H. H. Chen, Q. Qiao, M. S. J. Marshall, A. B. Georgescu, A. Gulec, P. J. Phillips, R. F. Klie, F. J. Walker, C. H. Ahn, S. Ismail-Beigi, *Nano Lett.* **2014**, *14*, 4965.
- [38] H. C. Du, *Ultramicroscopy* **2015**, *151*, 61.
- [39] M. Heidelmann, J. Barthel, L. Houben, *Ultramicroscopy* **2009**, *109*, 1447.
- [40] H. Y. Tan, J. Verbeeck, A. Abakumov, G. Van Tendeloo, *Ultramicroscopy* **2012**, *116*, 24.
- [41] M. Abbate, F. M. F. de Groot, J. C. Fuggle, A. Fujimori, O. Strelbel, F. Lopez, M. Domke, G. Kaindl, G. A. Sawatzky, M. Takano, Y. Takeda, H. Eisaki, S. Uchida, *Phys. Rev. B* **1992**, *46*, 4511.
- [42] T. Riedl, T. Gemming, K. Dörr, M. Luysberg, K. Wetzig, *Microsc. Microanal.* **2009**, *15*, 213.
- [43] P. Schattschneider, S. Rubino, C. Hébert, J. Ruzs, J. Kuneš, P. Novák, E. Carlino, M. Fabrizio, G. Panaccione, G. Rossi, *Nature* **2006**, *441*, 486.
- [44] Z. Q. Wang, X. Y. Zhong, R. Yu, Z. Y. Cheng, J. Zhu, *Nat. Commun.* **2012**, *4*, 1395.
- [45] T. Saltzmann, M. Bornhöfft, J. Mayer, U. Simon, *Angew. Chem. Int. Ed.* **2015**, *54*, 6632.
- [46] S. Estradé, J. Arbiol, F. Peiró, I. C. Infante, F. Sánchez, J. Fontcuberta, F. de la Peña, M. Walls, C. Colliex, *Appl. Phys. Lett.* **2008**, *93*, 112505.
- [47] M. J. Sayagués, J. M. Córdoba, F. J. Gotor, *J. Solid State Chem.* **2012**, *188*, 11.
- [48] R. D. Shannon, *Acta Crystallogr. A* **1976**, *32*, 751.
- [49] D. Meertens, M. Kruth, K. Tillmann, *J. Large-Scale Res. Facil.* **2016**, *2*, A60.
- [50] A. Thust, J. Barthel, K. Tillmann, *J. Large-Scale Res. Facil.* **2016**, *2*, A41.
- [51] R. Ishikawa, E. Okunishi, H. Sawada, Y. Kondo, F. Hosokawa, E. Abe, *Nat. Mater.* **2011**, *10*, 278.
- [52] D. E. Jesson, S. J. Pennycook, *Proc. R. Soc. London, A* **1995**, *449*, 273.
- [53] J. Barthel, L. Houben, K. Tillmann, *J. Large-Scale Res. Facil.* **2015**, *1*, A34.
- [54] M. Heggen, M. Luysberg, K. Tillmann, *J. Large-Scale Res. Facil.* **2016**, *2*, A42.
- [55] A. Kovács, R. Schierholz, K. Tillmann, *J. Large-Scale Res. Facil.* **2016**, *2*, A43.